

Performance evaluation of a medical robotic 3D-ultrasound imaging system

Marie-Ange Janvier ^{a,e}, Louis-Gilles Durand ^{b,e}, Marie-Hélène Roy Cardinal ^{a,e},
Isabelle Renaud ^a, Boris Chayer ^a, Pascal Bigras ^c, Jacques de Guise ^{c,e},
Gilles Soulez ^{d,e,f}, Guy Cloutier ^{a,e,f,*}

^a *Laboratory of Biorheology and Medical Ultrasonics, University of Montreal Hospital Research Center, Pavilion J.A. de Sève (room Y-1619), 2099 Alexandre de Sève, Montréal, Canada H2L 2W5*

^b *Laboratory of Biomedical Engineering, Clinical Research Institute of Montreal, University of Montreal, Montréal, Canada*

^c *Laboratory of Research on Imaging and Orthopaedics, University of Montreal Hospital Research Center and École de Technologie Supérieure, Montréal, Canada*

^d *Department of Radiology, University of Montreal Hospital, Montréal, Canada*

^e *Institute of Biomedical Engineering, University of Montreal, Montréal, Canada*

^f *Department of Radiology, Radio-Oncology and Nuclear Medicine, University of Montreal, Montréal, Canada*

Received 20 December 2006; received in revised form 12 October 2007; accepted 24 October 2007

Available online 1 November 2007

Abstract

3D-ultrasound (US) imaging systems offer many advantages such as convenience, low operative costs and multiple scanning options. Most 3D-US freehand tracking systems are not optimally adapted for the quantification of lower limb arterial stenoses because their performance depends on the scanning length, on ferro-magnetic interferences or because they require a constant line of sight with the US probe. Robotic systems represent a promising alternative since they can control and standardize the 3D-US acquisition process for large scanning distances without requiring a specific line of sight. The performance of a new prototype medical robot, in terms of positioning and inter-target accuracies (i.e., difference between measurements and ground truth values) was evaluated with a lower-limb mimicking phantom throughout the robot workspace. The teach/replay repeatability (i.e., difference between taught and replayed points) was also assessed. A mean positioning accuracy between 0.46 mm and 0.75 mm was found on all scanning zones. The mean inter-target distance accuracy varied between 0.26 mm and 0.61 mm. Teach/replay repeatability below 0.20 mm was also obtained. Additionally, a 3D reconstruction of in-vitro stenoses was performed with the robotic US scanner. The quantification error of a 80% area reduction (AR) stenosis was 3.0%, whereas it was -0.9% for a less severe 75% AR stenosis. Altogether, these results suggest that the robot may be of value for the clinical evaluation of lower limb vessels over long and tortuous segments starting from the iliac artery down to the popliteal artery below the knee.

© 2007 Elsevier B.V. All rights reserved.

Keywords: 3D-ultrasound imaging system; Cardiovascular imaging; Medical robotics; Robot accuracy; Robotics; Validation tool; Calibration phantom; Lower limb arterial diseases; Arterial stenoses; Radiology

1. Introduction

Atherosclerosis is the major cause of peripheral arterial disease (PAD), which leads to progressive narrowing of lower limb arteries (Golledge, 1997; Weitz et al., 1996). Atheromatous infiltration in PAD is usually diffuse with more than one stenosis affecting adjacent vessels. Different

* Corresponding author. Address: Laboratory of Biorheology and Medical Ultrasonics, University of Montreal Hospital Research Center, Pavilion J.A. de Sève (room Y-1619), 2099 Alexandre de Sève, Montréal, Que., Canada H2L 2W5. Tel.: +1 514 890 8000x24703; fax: +1 514 412 7505.

E-mail addresses: nicange18@aol.com (M.-A. Janvier), guy.cloutier@umontreal.ca (G. Cloutier).

PAD evaluation strategies are used in clinical practice. The ankle/brachial systolic blood pressure ratio measured with a cuff and a manometer is the oldest non-invasive index still utilized to assess the global disease of lower limb vessels (McDermott et al., 2002). Pulsed-wave Doppler ultrasound (US) and color Doppler flow imaging are the most popular non-invasive imaging techniques currently in use to investigate the severity of specific lesions along the lower limb vascular tree (Elsman et al., 1997; Matignon, 2002). Nevertheless, in most centers, a pre-intervention mapping by digital subtraction angiography (DSA), magnetic resonance angiography (MRA) or computed tomography angiography (CTA) is necessary to provide a complete 3D representation of the lower limb vessels to plan an appropriate therapy (Weitz et al., 1996). With these 3D imaging methods, the scan is performed over long segments usually starting from the abdominal aorta within the abdomen, following with iliac, femoral, and then with popliteal arteries to end in the tibial vessels of the calf. Although these imaging technologies yield high image resolution and 3D rendering, they still do not exhibit the same benefits of US that is low-cost, non-invasive, non-ionizing, safe and painless. Additionally, US presents multiple options for the diagnosis such as blood flow information with color Doppler, angiographic images with power Doppler and atherosclerotic plaque visualization with B-mode scanning. However, conventional 2D-US assessment of atherosclerotic disease highly depends on the observer (Delcker and Diener, 1994). As a result, many 3D-US systems were developed and validated in various clinical applications notably obstetrics, cardiology, and vascular imaging to increase the US diagnosis confidence (Nelson and Pretorius, 1998).

3D-US systems are based on two-dimensional arrays, mechanical localizers and freehand scanning with or without position sensing. Sensorless 3D-US systems include 2D linear array transducers (3D probes) (Bushberg et al., 2002), speckle decorrelation techniques (Fenster and Downey, 2000) and pseudo-tracking (Sonix, 2005). Only small volumes can be scanned using 3D probes. In speckle decorrelation techniques, the transducer is moved manually and speckle motion measurements are used to determine the distance between 2D images. The decorrelation algorithm used to predict the correct distance thus strongly relies on small constrained movement of the US probe. This technique can provide 3D-reconstruction if the image spacing is accurately determined and if the US transducer parameters are well known. Yet, since this approach does not guarantee accurate distances, it is not used to measure organ size, area nor volumes. Pseudo-tracking is an option available on many US systems today. This mode produces a 3D reconstruction from a 2D image sequence acquired during a manual linear scan. However, it does not provide an accurate 3D reconstruction since positions of 2D-US images are not tracked. Therefore, this approach is limited to scan regular geometries since a tortuous volume would be misrepresented as a linear one.

Sensor based 3D-US freehand systems include positioning information from tracking devices that are used to locate each 2D image in space and to reconstruct the sampled volume (Mercier et al., 2005). Optical tracking exploits properties of light to follow light emitting diode (LED) markers distributed on a rigid structure with charged coupled device (CCD) cameras. Electromagnetic (EM) tracking measures the magnetic field between a transmitter attached to the US probe and a receiver. Limitations of optical systems are mainly the requirement of a constant line of sight (Cartellieri et al., 2001; Rousseau, 2003), and those of EM sensors are errors induced by metallic object interference and a variable performance depending on the scanning distance (Birkfellner et al., 1998a,b; Frantz et al., 2003; Rousseau, 2003). Additionally, uneven volume sampling generated by the 3D-US freehand tracking method adds uncertainty to the reconstruction. Consequently, these devices are not well suited for lower limb vessel imaging, where the detection and quantification of long and tortuous arterial segments requires a high precision. In fact, a robust positioning accuracy of approximately 1 mm is likely needed for a tracking device to provide a competitive 3D-US quality analysis of stenoses in lower limb arteries.

Robotic systems represent a promising approach for stenosis quantification as they simultaneously control and standardize the 3D-US acquisition process for long scanning distances and complex geometries. Medical prototype robots have been developed to explore this advantage. For example, Hippocrate, a low-power robot actuated by slow stepper motors, is a force feedback medical robot that allows US and tonometry measurements with heart rate synchronization (Pierrot et al., 1999). While preliminary *in vivo* results looked promising, the main innovation of this system was the development of a force controller with design strategies selected to meet safety requirements imposed by medical applications. To our knowledge, no follow-up studies can be found on this robot in the literature. Furthermore, no evaluation of the robot accuracy has been performed. Other systems such as an image-guided control instrument (Abolmaesumi et al., 2002) and a tele-robot (Gonzales et al., 2001) were developed for 3D-US scanning. The first system was designed for the tele-examination of carotid arteries on short rectilinear paths. The control of the US probe movement is shared between the operator, the robot controller and the US image processor. This system produces autonomous tracking of the vessel contour in real-time scans to compensate for the physiological motion of an artery during probe motion along a 1D trajectory. Thus, the US probe movement is controlled in three degrees of freedom (DOF) that are constrained to lie in the US observation plane. Nevertheless, this robot operates within a limited range in the robot workspace and is restricted to straight line objects of interest (i.e., no tortuous curved objects) to obtain visual information. Certainly, the principal accomplishments of this robot remain the development of ultrasound visual servoing and control that enable a remote assistance for tele-

operation. The second design is a tele-robotic system also with remote control assistance to facilitate hand-eye coordination necessary to perform echographic examination over the abdomen of pregnant women. It is to note that most developments have been so far oriented towards architectural control and safety designs. However, it is very important that new medical hardware and software designs be validated to meet specific clinical needs.

To provide accurate 3D US scanning of lower limb vessels, a prototype medical robot was recently developed by our team. A teach mode that enables the learning of a “freehand” scan, and a replay mode to reproduce the manually taught path are available. These features, which are also present in Hippocrate, accommodate specific scan routes with controlled speed. In addition, when coupled to an US probe, the system captures and stores images with their registered 3D spatial location at uniform spacing in replay mode. Furthermore, the robot was designed to have a constant high accuracy over its entire workspace. Thus, a clinician can integrate their regular scanning operation for each patient’s leg by manually teaching a scan path to the robot. The robot replays the path over the leg and acquires 2D images for 3D reconstruction. The reconstructed vessel segments consequently remain within the US image plane obtained on a pre-determined trajectory for each patient scan. A sub-objective of this study was to use a double-stenosis vascular phantom to evaluate the feasibility of accurate quantification of stenoses in 3D with the prototype robotic scanner.

2. Materials

2.1. Prototype medical robot

The robot includes three principal components: the computer workstation, the robotic arm and the US scanning system. An overview of this system is shown in Fig. 1. The robotic arm is managed through a custom made software installed on the computer workstation. Namely, the robotic arm carries the US probe to scan a volume.

Then, B-mode images are acquired with corresponding probe positions for 3D-reconstruction.

The URS software (Ultrasound Robotic Scanner, Integral Technologies Inc., Laval, Québec, Canada), which runs on the workstation, provides a user interface to access and set-up the robot controls, movements, parameters and tasks. This specialized software was developed in Visual C++ and run under Windows. This higher control architecture allows three operative states for the robotic arm: teach, replay and idle modes. In teach mode, the operator manually moves the robotic arm while the robot controller uploads the real time arm positions to the workstation; the positions are then saved in a trajectory file. Thereafter, in replay mode, the saved trajectory file is sent back to the robotic arm into movement commands. The replayed trajectory is executed at constant speed and contact pressure with the patient or object to be scanned. The last robot arm state is the idle mode where the operator can freely handle manually the arm without trajectory file processing. Also, the software limits any tool attached to the robotic arm to a maximum linear speed of 50 mm/s in addition to a maximum applied force (i.e., 100 N in the normal direction and 50 N in the transverse directions). Finally, the workstation communicates with the robot controller according to the RS-232 protocol.

The robot controller (CRS C500C, CRS Robotics Corporation) provides safety circuits, power and motion control for the robotic arm. It drives the motors in each joint, keeps track of motor position through feedback from encoders, computes trajectories and stores robot applications in memory. The modules implemented in the robot controller consist of the lower architecture control level. These modules were all written in the RAPL-3 programming language. They translate the position commands and move the arm as requested by the workstation. Additionally, the robot controller triggers the image acquisition and sends the corresponding arm position to the workstation.

The robotic arm is an industrial robot (F3 Articulated Robot, CRS Robotics Corporation, Burlington, Ontario,

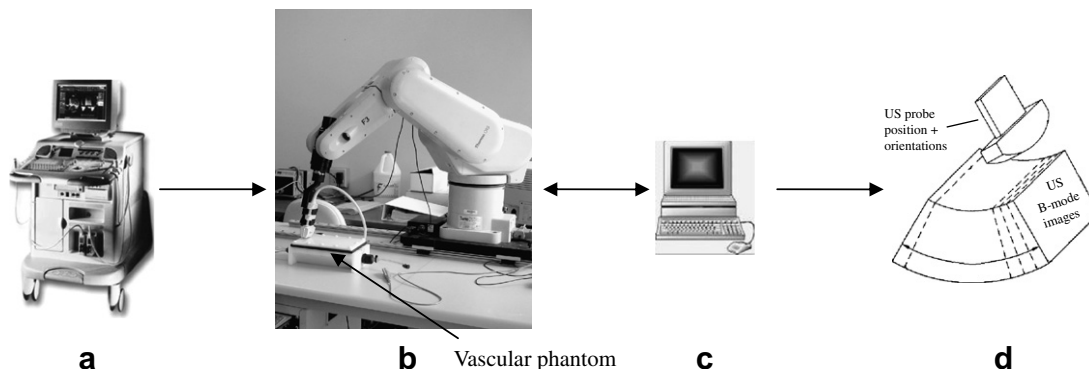


Fig. 1. The 3D-ultrasound (US) robotic imaging system. The F3 CRS robotic arm (b) carries a probe from an US system (GE Vivid-5) (a). The robotic arm is moved through the user interface software on the workstation (c). 2D US images are tagged with the US probe positions acquired from the robotic arm (d). In this example, a vascular phantom is scanned.

Canada). Note that many groups have used CRS industrial robots to develop specialized light-weight precision tasks. In particular, medical applications include image-guided surgery (Tseng et al., 2007) and 3D transrectal ultrasound-guided prostate brachytherapy (Zhouping et al., 2005). Our industrial manipulator is an articulated robotic arm designed for light payload applications (3 kg). Moreover, applications that require complex and flexible movements are recommended for this particular model. Our unit has 6 DOF with absolute encoders in each arm joint that provide continuous information on the arm stance and position to the robot controller. In our system, the robotic arm moves the US probe with commands from the workstation and information that comes from the force/torque sensor.

The force/torque sensor (F/T) (ATI, Industrial Automation, Apex, NC, USA) connected to the robotic arm is a key element of the 3D US scanner system. This sensor allows easy handling and precise positioning of the robot manipulator by the operator. Manual handling of the robotic arm is possible because the F/T sensor reports all forces and torques applied to the robot controller. This information is then transmitted to the workstation where forces and torques are converted into positioning information to move

the arm and generate the trajectory file in teach, replay and idle modes. Additionally, in replay mode, the workstation employs force feedback. This is performed with repetition of the same applied US probe pressure to the patient and safe monitoring of the threshold contact force.

The robotic system assures patient security through many safety controls. Two control schemes of watchdog mechanisms were added to the system in case of failure: one at the customized software and the other at the robot controller. The watchdog monitors continuous digital signals sent from the robot controller and the workstation. If the robot controller or workstation goes out of control or does not respond, the emergency stop (E-stop) is activated. Its activation immediately removes power from the robotic arm and fail-safe brakes are automatically engaged to prevent movements due to gravity. Moreover, the software monitors singularities of joint configurations, joint limits and tracks errors between desired and current positions. Furthermore, there is a maximum limit set for the US probe pressure and linear scanning speed. Also, three additional E-stop buttons, which can be manually triggered, are available in the robot operating workspace. Other safety designs include the operator button that needs to be pressed throughout the entire replay mode to ensure

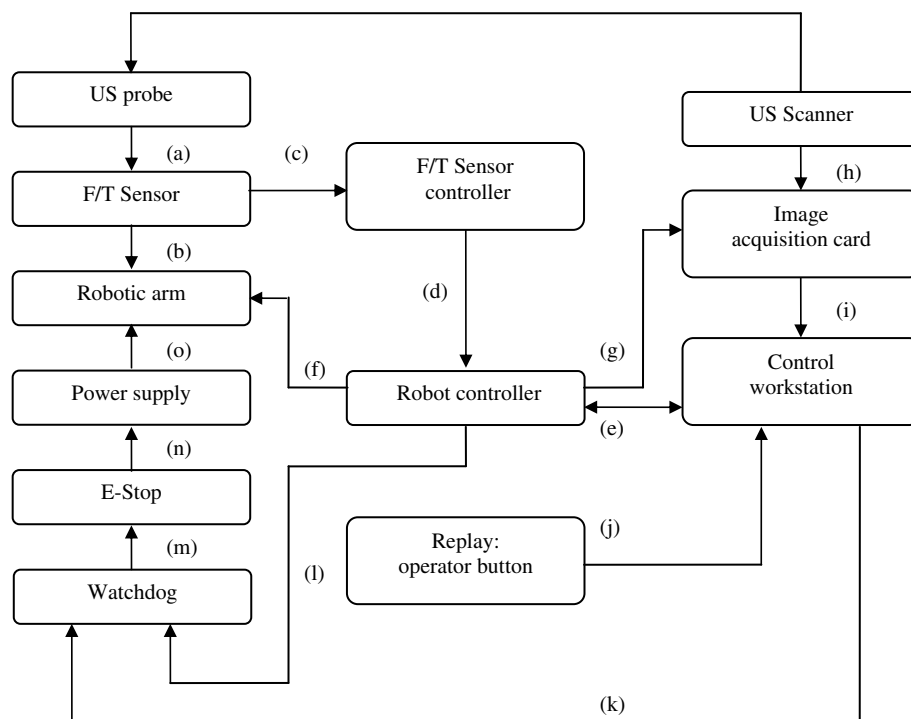


Fig. 2. The 3D-ultrasonic robotic system block diagram. The US probe is attached to the force/torque (F/T) sensor (a) incorporated in the robotic arm (b). In teach mode, forces and torques applied to the sensor are sent to the F/T sensor controller (c) then to the robot controller (d). The robot controller translates forces and torques into positioning information that are transmitted and saved into the control workstation (e). In replay mode, the workstation transfers the saved trajectory to the robot controller (e). The robot controller translates this trajectory into robotic positions and commands the robotic arm to move (f). At the same time, the robot controller uploads in real time the US probe location to the control workstation (e) and triggers the image acquisition card (g). 2D images are thus simultaneously acquired from the US scanner (h) and saved into the control workstation (i). Safety control is assured in replay mode with the operator button that monitors the robot movements and sends the information to the control workstation (j). Additionally, if any of the control workstation (k) or the robot controller modules fail (l), a watchdog mechanism activates the emergency stop (m) (E-stop). The E-stop activation automatically removes (n) all the power supplied to the robotic arm (o).

the monitoring of the replayed trajectory. It is to note that the Hippocrate robot as well contains similar security features (Pierrot et al., 1999).

The last principal component is the US scanner. It provides images of a scanned volume in any available modalities (e.g., B-mode, color Doppler, power Doppler). Any US scanner for which it is possible to attach the US probe to the F/T sensor handle on the robotic arm can be used. In its current form, the robotic system provides its own digitization of US images. 2D-US images are captured at uniform spacing with an image acquisition card (PCI-1411, National Instrument, Austin, Texas, USA) mounted in the workstation. These US images are then digitized in 480×640 pixels format from the scanner video output. Simultaneously, US probe positions of the robotic arm are associated to the acquired 2D-US images and saved into the workstation for 3D-reconstruction. Fig. 2 shows the complete 3D-US robotic system block diagram.

2.2. Phantom model

A phantom was specially designed to assess the accuracy of the robot arm to position a spherical pointer (SP) within holes manufactured on a leg mimicking geometry. Fig. 3 shows the phantom where dimensions correspond to the upper half of a thigh and where holes are arranged in three different paths. The paths match classical US lower limb

vessel scanning trajectories. They were designed in linear, arc and curved fashions (see Fig. 3). Paths 1, 2 and 3 contain 15, 6 and 16 holes, respectively. Each hole was manufactured with a precision of 0.03 mm, a 8.38 mm diameter and a 4.19 mm depth. To avoid redundancy in the 3D space explored by the SP, the phantom was designed without collinear and coplanar points.

The SP at the robot end-effector replaced the US probe for the accuracy and teach/replay repeatability testing. Fig. 4 shows the SP added to the robotic arm where the spherical end fits tightly within the phantom holes. Various orientations were possible when the SP was in contact with the phantom target points. Even though the center of the

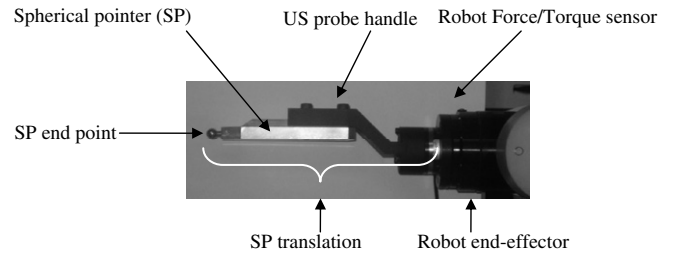


Fig. 4. The spherical pointer used to determine the performance of the robotic US scanner. The SP is rigidly attached to the US probe handle that is linked to the robot end-effector. The SP translation is a vector that is estimated to make the SP center of gravity known in the robot referential.

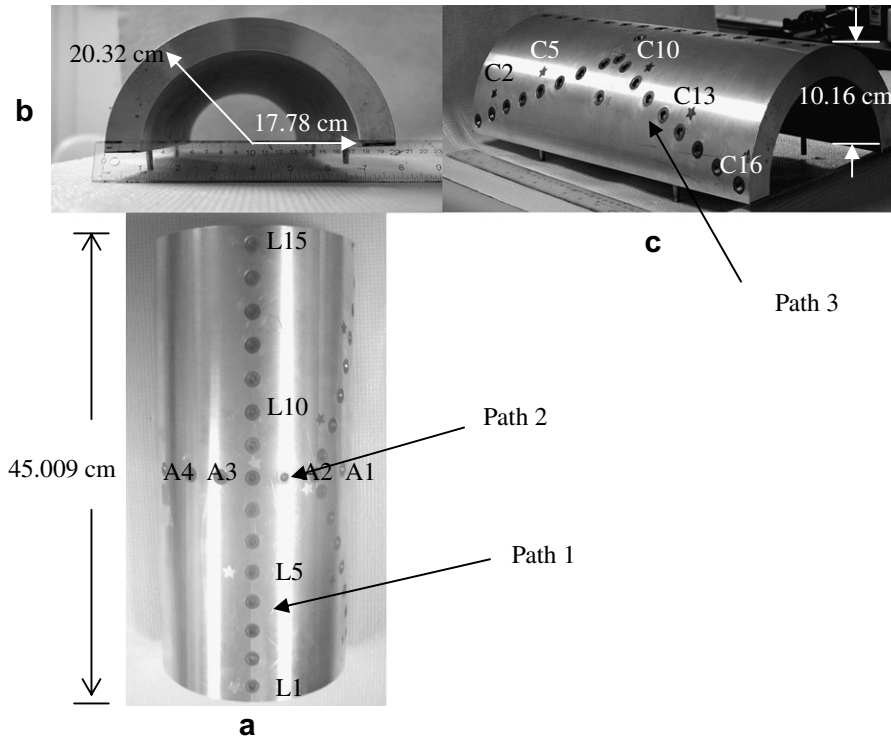


Fig. 3. The lower limb mimicking phantom, top (a), axial (b) and side (c) views. The three paths represent classical lower limb vessel scanning trajectories. The phantom contains a total of 37 holes which serve as target points for the robotic spherical pointer (SP, see Fig. 4). A total of 13 holes were selected for the accuracy and teach/replay repeatability measurements. Path 1 is linear with four selected targets (L1, L5, L10 and L15). Path 2 represents the arc path with four selected targets (A1, A2, A3 and A4) and path 3 is curved with five targets (C2, C5, C10, C13 and C16). Each target point is labeled according to the corresponding path: L for linear, A for arc and C for curved.

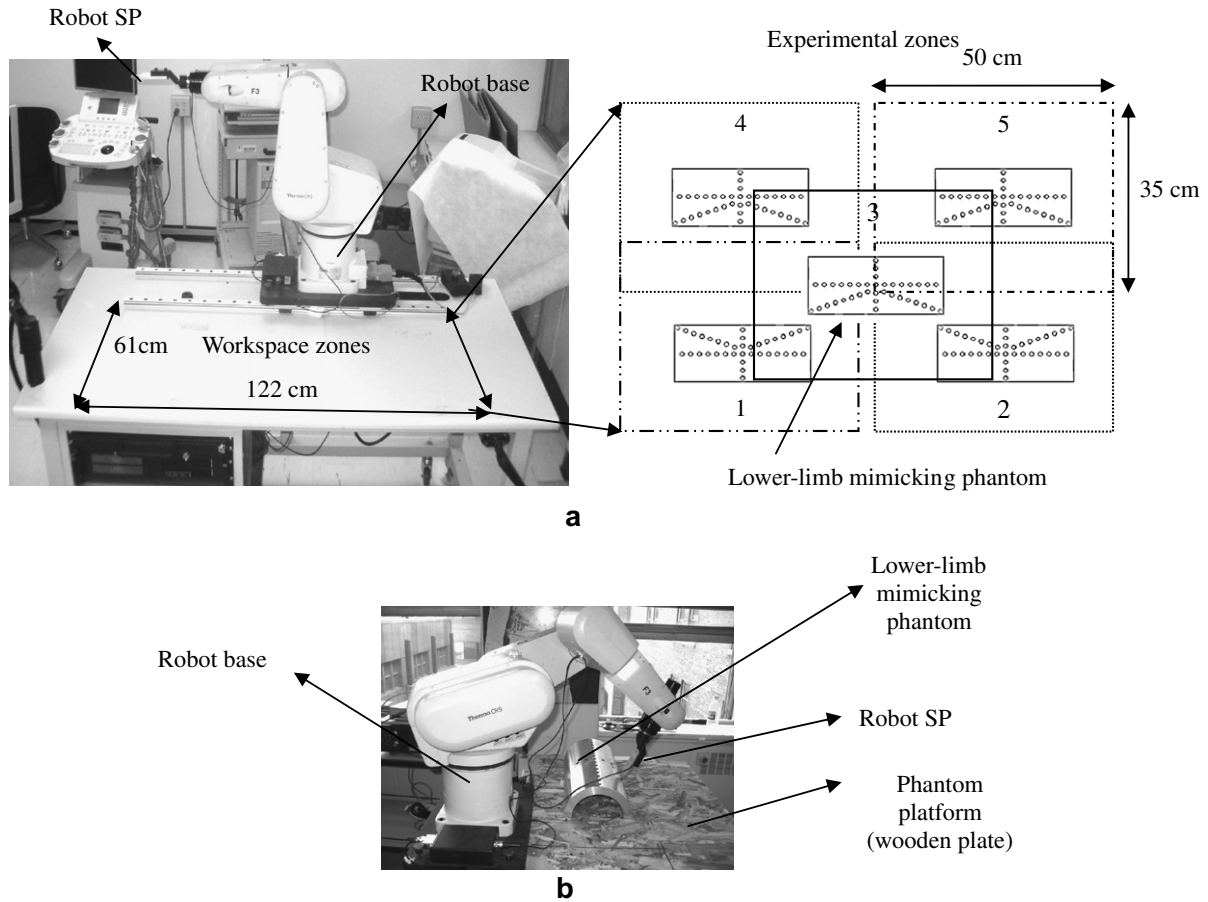


Fig. 5. (a) The designated experimental zone in the robot workspace. The lower-limb mimicking phantom was positioned in five different zones where the patient leg is most likely to be placed. (b) The phantom rigidly attached to the platform (wooden plate) with the robot spherical pointer (SP) inserted in one of the semi-spherical holes micro-machined in the phantom.

SP was constrained to the center of a phantom hole, infinite configurations of the robot joints were possible. This method, also referred as the single endpoint contact method, is usually the preferred approach for robot calibration (Mavroidis et al., 1998; Mooring et al., 1991).

The phantom was centrally positioned and fixed within each of five designated experimental zones in the robot workspace, as illustrated in Fig. 5. The orientation of the leg phantom in each experimental zone is given as well in Fig. 5a. The experimental zones were chosen to allow the identification of optimum operating areas in the robot workspace. Likewise, selected zones and phantom orientations were chosen to correspond to the expected scan positions of a patient lower limb during a clinical exam.

3. Methods

In order to evaluate the robot performance, the methods required to relate the coordinate system of the robot, to that of SP and of the phantom, as identified in Fig. 6. Because the SP was not considered in the robot referential, a calibration procedure was thus needed to determine the SP center of gravity with respect to the robot referential.

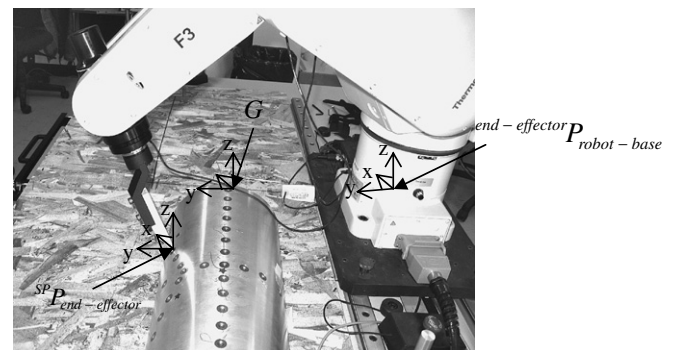


Fig. 6. The three referential coordinate systems in this study: the robot end-effector $P_{robot-base}$, the spherical pointer (SP) $SP P_{end-effector}$ and the phantom G .

Thereafter, the performance of the robot could be evaluated with the SP. It was quantified in terms of positioning and inter-distance accuracies (i.e., difference between measurements and ground truth values) with the phantom target points, and in term of teach/replay repeatability of the measures (i.e., difference between ‘teach’ and ‘replay’ points).

3.1. SP calibration

The robot reports the Cartesian position and orientation of its last joint or wrist, also referred as the end-effector. The SP coordinates could be transformed with respect to the base of the robot because the orientation and position of the end-effector were known. To perform the SP calibration, its translation with respect to the end-effector was calculated by using the following equation (Detmer et al., 1994; Hartov et al., 1999; Leotta et al., 1997)

$${}^{\text{SP}}P_{\text{robot-base}} = {}^{\text{end-effector}}P_{\text{robot-base}} + ({}^{\text{end-effector}}R_{\text{robot-base}} \times {}^{\text{SP}}P_{\text{end-effector}}), \quad (1)$$

where ${}^{\text{SP}}P_{\text{robot-base}}$ defines the unknown position vector of the SP center of gravity with respect to the robot referential, ${}^{\text{end-effector}}P_{\text{robot-base}}$ represents the known position vector of the robot end-effector in the base referential, ${}^{\text{end-effector}}R_{\text{robot-base}}$ describes the known Euler rotation matrices that transform the end-effector orientation in the robot referential, and ${}^{\text{SP}}P_{\text{end-effector}}$ is the unknown translation vector of SP in the end-effector referential. The positions P are 3×1 vectors and the rotation matrix R is 3×3 . When a specific phantom target hole is reached several times with different tool configurations, Eq. (1) becomes over determined. Unknowns can thus be solved using the least-square method. Once the SP vector ${}^{\text{SP}}P_{\text{end-effector}}$ was estimated, the SP position for following experiments could be calculated in the robot referential with Eq. (1).

To perform the SP calibration, the robot arm was operated manually in idle mode. In each experimental zone of the robot workspace, two holes on phantom path 1 were randomly selected. For each hole and zone, the SP was rotated manually to 32 different positions distributed in a hemispherical pattern around each selected phantom target pivot. Cartesian position and orientation of the robot end-effector were then recorded for each SP configuration. The ${}^{\text{SP}}P_{\text{end-effector}}$ vector was estimated with Eq. (1) for each experiment (2 phantom holes in each of five robot workspace zones for a total of 10 estimated SP translations). The mean value of this vector was used as the SP translation for subsequent performance assessments.

3.2. SP calibration precision

A precision metric was evaluated since subsequent performance measurements to be reported below also depend on the SP translation precision. The precision was defined as the ability to locate the same point in space with small position variations. Since it is not physically possible to locate the origin of the robot coordinate system because it is inside the robot base, it was not possible to accurately measure the location of any object in the base coordinate system using rulers (Barratt et al., 2001; Frantz et al., 2003; Hartov et al., 1999). Thus, a point position acquired with the robot could not be compared with its true physical location. The SP precision \bar{s} was computed by using

$$\bar{s} = \frac{1}{TLM} \sum_{i=0}^T \sum_{j=0}^L \sum_{k=0}^M \sqrt{\sigma_{x_{i,j,k}}^2 + \sigma_{y_{i,j,k}}^2 + \sigma_{z_{i,j,k}}^2}, \quad (2)$$

where $\sigma_{x_{i,j,k}}^2$ is the variance for $T = 10$ SP calibration configuration positions i in the x direction for the experimental zone j and target point k . This definition applies as well for the y and z directions. The average precision was calculated for $L = 5$ zones, $M = 2$ target holes randomly chosen among the selected path 1 (see Fig. 3a for the selected target point options) for a total sample size of 100 points. It is to note that the data collected for the SP calibration was not used to assess the average SP precision.

3.3. Performance evaluation of the robot

The relative positioning accuracy, the inter-distance accuracy, and the teach/replay repeatability in locating the SP were assessed. The robot referential first needed to be transformed into the phantom coordinate system, as described earlier by Eq. (1). For that purpose, the position of the selected phantom points indicated in the legend of Fig. 3 was acquired with four different SP orientations randomly chosen ($T = 4$ in this case); a sample mean was computed for each target point. These mean values corresponded to the phantom theoretical central positions of the holes in the robot referential. In the phantom coordinate system, the ground truth position of each hole was known from the computer-assisted-design (CAD) file used to manufacture the mimicking leg. The translation offset between the phantom ground truth and the theoretical target points in the robot referential was then calculated. The offset ${}^{\text{phantom}}\text{offset}_{\text{robot-base}}$ was determined for all selected target points in each zone and it was averaged to obtain the position of the phantom with respect to the robot base. The translation value is different in each zone and consequently it had to be recomputed when the phantom was moved. With ${}^{\text{phantom}}\text{offset}_{\text{robot-base}}$ known in each zone, the phantom points targeted with the robot arm could be transformed into the phantom referential by using

$${}^{\text{phantom}}P_{\text{robot-base}} = {}^{\text{SP}}P_{\text{robot-base}} + {}^{\text{phantom}}\text{offset}_{\text{robot-base}}, \quad (3)$$

where ${}^{\text{phantom}}P_{\text{robot-base}}$ defines the 3×1 position vector of the center target point of the hole acquired with the robot and transformed into the phantom coordinate system, ${}^{\text{SP}}P_{\text{robot-base}}$ is the 3×1 position vector of the SP center of gravity with respect to the robot referential, and ${}^{\text{phantom}}\text{offset}_{\text{robot-base}}$ is the 3×1 translation offset vector to position the robot base in the phantom referential. It can be recalled that Fig. 6 illustrates the three referential objects of this study: the robot, the phantom and the SP.

3.3.1. Positioning and inter-distance accuracies

The robot positioning and inter-distance accuracies were evaluated with the leg mimicking phantom on a total of 13 target points (see Fig. 3). The same targets were evaluated in each robot experimental zone and for each hole, taught and replayed data were collected. In teach mode, the oper-

ator manually moved the SP to a phantom target point. The robot arm then replayed the taught path to reach the same target. Data collection consisted of the Cartesian position and orientation of the robot end-effector (using $T = 4$, as mentioned earlier). The robot end-effector position and orientation for all collected data were transformed into the robot referential with Eq. (1). Data positions were then transformed from the robot referential into the phantom coordinate system with Eq. (3).

The relative positioning accuracy \overline{Ps} , calculated with Eq. (4), is the mean distance between the phantom ground truth point positions and the phantom points collected with the robot SP and transformed in the phantom referential. The inter-distance accuracy $\overline{IntDist}$, given by Eq. (5), evaluates the robot error in segment length measurements; it is the mean absolute error between the length separating phantom ground truth neighbor points and the length separating the corresponding target points collected with the robot SP:

$$\overline{Ps} = \frac{1}{TM} \sum_{i=0}^T \sum_{k=0}^M \|G^k - \text{phantom} P_{\text{robot-base}}^{i,k}\|, \quad (4)$$

$$\overline{IntDist} = \frac{1}{T(M-1)} \sum_{i=0}^T \sum_{k=1}^{M-1} \| \|G^{k+1} - G^k\| - \| \text{phantom} P_{\text{robot-base}}^{i+1,k+1} - \text{phantom} P_{\text{robot-base}}^{i,k} \| \| . \quad (5)$$

In Eqs. (4) and (5), G^k defines the 3×1 ground truth position vector of target point k obtained from the CAD file of the designed phantom, $\text{phantom} P_{\text{robot-base}}^{i,k}$ describes the 3×1 robot target point position vector transformed into the phantom referential of target point k for the SP configuration i , $T = 4$ corresponds to the different SP configurations taken around the target point, and $M = 13$ is the number of selected phantom target points. \overline{Ps} and $\overline{IntDist}$ were evaluated in each robot workspace zone ($L = 5$). The inter-distance accuracy $\overline{IntDist}$ was computed for only neighbor target points pair in a specific path (e. g., in path 1, inter-distance pairs included L1-L5, L5-L10 and L10-L15). As a result, a smaller data sample was used for this evaluation.

3.3.2. Teach/replay repeatability

The teach/replay repeatability is the distance between the robot teach and replay points. It was assessed with the data collected for the robot accuracy measurements. For this analysis, it was not necessary to know the translation of the data in the phantom coordinate system; the collected data were only transformed into the robot referential with Eq. (1). The teach/replay repeatability \overline{Rpt} was calculated with:

$$\overline{Rpt} = \frac{1}{TM} \sum_{i=0}^T \sum_{k=0}^M \| \text{SP} P_{\text{robot-base}}^{\text{teach}, i,k} - \text{SP} P_{\text{robot-base}}^{\text{replay}, i,k} \| \quad (6)$$

where $\text{SP} P_{\text{robot-base}}^{\text{teach}, i,k}$ is the teach position vector with respect to the robot referential of target point k for the SP configuration i , $\text{SP} P_{\text{robot-base}}^{\text{replay}, i,k}$ represents the replay position vector with respect to the robot referential of target point k for the SP configuration i , $T = 4$ is the number of SP configurations, and $M = 13$ is the number of target points. \overline{Rpt} was evaluated in each robot workspace zone ($L = 5$).

3.3.3. Statistical analyses

Multiple pairwise comparisons with Bonferonni tests were performed on accuracy and teach/replay repeatability results to evaluate differences among the robot operating zones and phantom paths. All statistical analyses were performed with the SPSS statistical software (version 13.0, SPSS Inc., Chicago, IL).

3.4. 3D-US reconstruction of a vascular phantom from a robot scan

The performance of the 3D-US robotic system for the reconstruction of a vessel was evaluated by using a symmetric cylindrical vascular phantom of known length with two consecutive stenoses of 80% and 75% area reductions. The fabrication phantom ground truth values were obtained from micro-caliper measurements performed on the low-melting point vessel lumen prototype. Fig. 7 shows the vascular phantom box and lumen mold. A complete description of the fabrication process, characteristics and

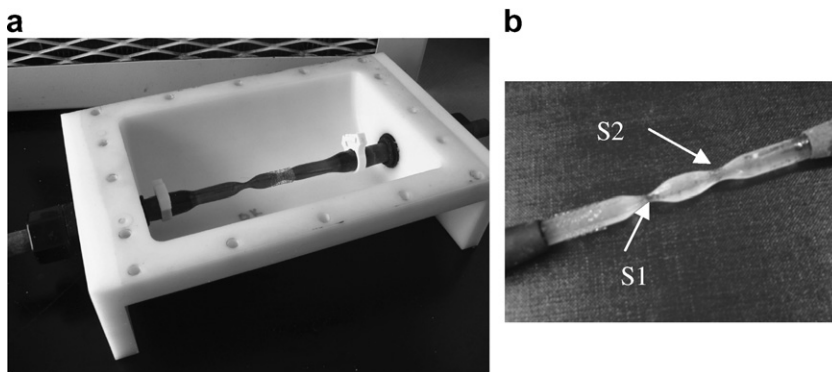


Fig. 7. The symmetric cylindrical vascular phantom. (a) The lumen mold of the vascular phantom with double stenoses is shown without the box top cover and the agar-mimicking tissue material used to fill the phantom. (b) A view of the lumen mold alone is shown, labels S1 and S2 correspond to the first and second stenoses with 80% and 75% area reductions, respectively. The sugar-based lumen mold is removed when the fabrication process is completed by introducing the phantom in water. This allows producing a vessel with two stenoses that is filled with degassed water for ultrasound scanning.

geometric accuracy of the phantom is available in (Cloutier et al., 2004). For the current evaluation, the vascular phantom was placed in zone 3 of the robot workplace (see Fig. 5) and scanned along its length. The robotic system was coupled to an US scanner equipped with a 10 MHz linear array probe (Model FPA, Vivid-5 US system, General Electric, Chicago, IL, USA). In order to reconstruct the vascular phantom accurately, a 3D-US calibration was first performed by using a cross-wire phantom. Thereafter, the quantification of the diameter and area reduction of stenoses was performed on the reconstructed volume obtained from US images captured with the robot system.

3.4.1. Calibration with a cross-wire

To locate US images within the robot coordinate system, it was necessary to find the transformation (rotation and translation) of the US image plane with respect to the probe position. This was achieved with a cross-wire calibration phantom made with two crossed threads suspended in water. Several scans were performed with a wide range of US probe angles and positions. The intersection of the two wires was aligned in the US image for a specific depth. The center of the intersection was manually segmented and considered as the origin of the phantom coordinate system to solve the following equation (Mercier et al., 2005):

$$\begin{pmatrix} 0 \\ 0 \\ 0 \\ 1 \end{pmatrix} = T_{\text{robot-base}}^{\text{phantom}} \cdot T_{\text{USprobe}}^{\text{robot-base}} \cdot T_{\text{image}}^{\text{USprobe}} \cdot \begin{pmatrix} s_x \cdot u_k \\ s_y \cdot v_k \\ 0 \\ 1 \end{pmatrix}, \quad (7)$$

where $T_{\text{robot-base}}^{\text{phantom}}$ is the unknown transformation (rotation and translation) of the cross-wire phantom with respect to the robot referential, $T_{\text{USprobe}}^{\text{robot-base}}$ represents the known transformation of the US probe with respect to the robot referential for an acquired image, and $T_{\text{image}}^{\text{USprobe}}$ is the unknown transformation of the image with respect to the US probe. For each image k , u_k and v_k represent the column and row indices with respect to the B-scan origin; s_x and s_y are defined as the scaling parameters in mm/pixel estimated from the B-scan depth settings. A Levenberg–Marquadt iterative algorithm was employed to compute the unknown parameters since the cross-wire position is undefined in the robot referential. Once the calibration matrix $T_{\text{image}}^{\text{USprobe}}$ is determined, all cross-wire points in the acquired images were reconstructed in the robot referential with Eq. (7) to assess the calibration precision C_{rms} :

$$C_{\text{rms}} = \sqrt{\frac{\sum_{i=1}^N \sigma_i}{N}}, \quad (8)$$

where σ_i is the standard deviations of the reconstructed points for an US image i among a total of N images.

3.4.2. 3D-US reconstruction

A US scan with quasi-parallel planes of the phantom was taught and replayed by the robot. B-mode images

(480 × 640 pixels) were captured, digitized and stored on the workstation. Images were cropped to a region of interest and then segmented by using a fast-marching method based on gray level statistics and gradients adapted from (Roy Cardinal et al., 2006). It provided an outline of the phantom vessel wall boundary. Each segmented contour pixel position (u_k, v_k) was then mapped to the reconstruction volume B with the calibration matrix $T_{\text{image}}^{\text{USprobe}}$, their respective scaling factors (s_x, s_y) and with the corresponding US probe transformation parameters $T_{\text{USprobe}}^{\text{robot-base}}$. Thus, each pixel x^B of the 3D surface reconstruction was expressed by the following equation:

$$x^B = T_{\text{USprobe}}^{\text{robot-base}} \cdot T_{\text{image}}^{\text{USprobe}} \cdot \begin{pmatrix} s_x \cdot u_k \\ s_y \cdot v_k \\ 0 \\ 0 \end{pmatrix}. \quad (9)$$

The transformed contours were re-sampled on a rectangular grid and interpolated to provide a 3D surface rendering.

3.4.3. Quantification of stenoses

Stenoses were evaluated from the 3D-reconstruction. The reconstructed volume was re-sliced perpendicularly to the longitudinal axis of the vessel. A mean diameter and an area were computed for each cross-section. From this data set, 10 samples in regions where the area was maximum were used to compute the average dimension of the reference vessel A_{ref} . In regions where the area was minimum (within stenoses), one value was used to compute the average diameter and area of the reduced stenosis A_{min} . Stenoses in the 3D volume were quantified according to the following equation:

$$\% \text{ of reduction} = 100 \times \left(\frac{A_{\text{ref}} - A_{\text{min}}}{A_{\text{ref}}} \right). \quad (10)$$

The quantification error for both stenoses was determined and compared to the fabricated phantom ground truth values obtained from micro-caliper measurements.

4. Results

4.1. SP calibration

The SP translation magnitude ${}^{\text{SP}}P_{\text{end-effector}}$ in Eq. (1) was estimated as 194.33 ± 0.36 mm. The corresponding translation position coordinates, which represent the SP center of gravity in the x , y and z directions with respect to the robot end-effector, are listed in Table 1.

4.2. SP calibration precision

The mean SP precision according to Eq. (2) was found to be 0.57 ± 0.30 mm for the five experimental zones. This mean was calculated with 100 collected points in the robot workspace. Fig. 8 presents the histogram of the distance between each target position acquired with the SP and the corresponding mean target position. Most data

Table 1
Spherical pointer (SP) calibration results

${}^{\text{SP}}P_{\text{end-effector}}$	Position vector			Magnitude $\ {}^{\text{SP}}P_{\text{end-effector}}\ $
	X	Y	Z	
Mean (mm)	-12.05 ± 0.64	-1.38 ± 0.27	194.50 ± 0.35	194.33 ± 0.36

${}^{\text{SP}}P_{\text{end-effector}}$ is the estimated translation vector of the SP in the end-effector referential.

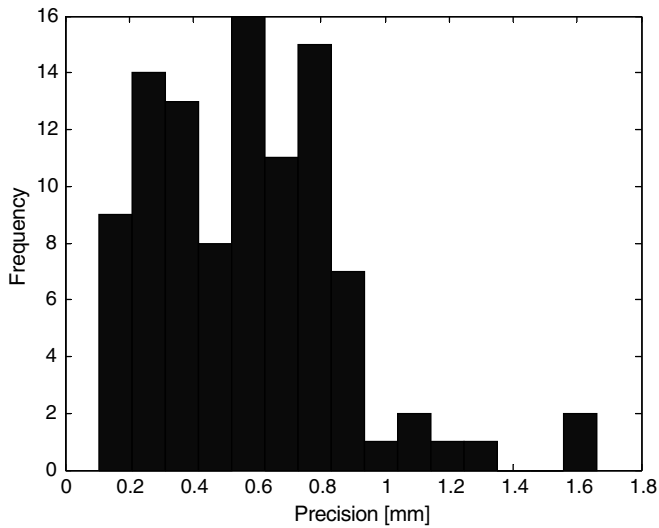


Fig. 8. The precision histogram of the robot scanner determined by using the spherical pointer. For the five experimental zones, a mean of 0.57 ± 0.30 mm was found.

acquired at different angulations of the SP resulted in a precision below 1 mm.

4.3. Performance evaluation

4.3.1. Positioning accuracy

The mean relative positioning accuracy calculated with Eq. (4) was 0.60 ± 0.29 mm in teach mode, while it was 0.62 ± 0.29 mm in replay mode. Ninety five percent of the data points (248 instead of 260 samples) was collected in teach and replay modes given that some holes were not reachable by the robot. Table 2 details the positioning accuracy within each designated experimental zones and different phantom paths for teach and replayed points. Statistically significant differences were found between the robot experimental zones ($p < 0.05$) for both $\overline{P}_{\text{steach}}$ and $\overline{P}_{\text{sreplay}}$ measurements. The pairwise comparisons revealed a significantly higher positioning error in zone 1 compared to zones 2 and 5 ($p < 0.001$ and $p < 0.05$, respectively). Furthermore, over all robot workspace zones and for both

Table 2
Robot positioning accuracy

Experimental zones	Phantom paths	$\overline{P}_{\text{steach}}$ (mm)	$\overline{P}_{\text{sreplay}}$ (mm)	Sample size (N)
Zone 1	1	$0.69 \pm 0.26^*$	$0.69 \pm 0.28^*$	12
	2	0.74 ± 0.33	0.75 ± 0.33	16
	3	$0.69 \pm 0.30^*$	$0.70 \pm 0.30^*$	16
	Mean	0.71 ± 0.29 ξ, δ	0.72 ± 0.30 ξ, δ	44
Zone 2	1	$0.46 \pm 0.27^*$	$0.59 \pm 0.30^*$	16
	2	0.46 ± 0.18	0.49 ± 0.19	16
	3	$0.55 \pm 0.28^*$	$0.60 \pm 0.29^*$	20
	Mean	0.50 ± 0.25 ξ	0.56 ± 0.27 ξ	52
Zone 3	1	$0.48 \pm 0.19^*$	$0.47 \pm 0.18^*$	16
	2	0.64 ± 0.26	0.60 ± 0.28	16
	3	$0.72 \pm 0.35^*$	$0.73 \pm 0.34^*$	20
	Mean	0.62 ± 0.29	0.61 ± 0.29	52
Zone 4	1	$0.61 \pm 0.27^*$	$0.61 \pm 0.27^*$	16
	2	0.52 ± 0.29	0.49 ± 0.25	16
	3	$0.72 \pm 0.37^*$	$0.75 \pm 0.42^*$	20
	Mean	0.63 ± 0.32	0.63 ± 0.34	52
Zone 5	1	$0.54 \pm 0.25^*$	$0.56 \pm 0.22^*$	16
	2	0.63 ± 0.21	0.62 ± 0.23	16
	3	$0.56 \pm 0.24^*$	$0.55 \pm 0.22^*$	16
	Mean	0.58 ± 0.23 δ	0.58 ± 0.22 δ	48
All zones	Total mean	0.60 ± 0.29	0.62 ± 0.29	248

\overline{P}_{s} is the relative mean positioning accuracy which defines the mean distance between ground truth and robot measured phantom points. It was calculated in the robot teach ($\overline{P}_{\text{steach}}$) and replay ($\overline{P}_{\text{sreplay}}$) modes. δ and ξ indicate statistically significant differences between experimental zones from pairwise comparisons with $p < 0.05$ and $p < 0.001$, respectively.

* Signifies that a statistically significant difference between paths was found over all robot workspace zones for both teach and replay modes with $p < 0.05$.

\overline{Ps}_{teach} and \overline{Ps}_{replay} , a statistically significant difference between phantom paths 3 and 1 was found ($p < 0.05$) with the smallest error in the linear path (path 1). However, no statistically significant difference was found between the teach and replay positioning accuracy over all zones and phantom paths ($p = 0.67$).

4.3.2. Inter-distance accuracy

The mean inter-distance accuracy computed with Eq. (5) in teach mode ($\overline{IntDist}_{teach}$) was 0.43 ± 0.32 mm, whereas for the replay mode, $\overline{IntDist}_{replay}$ was 0.42 ± 0.33 mm. Seventy eight percent (188 over 240 holes) of the data points was used for the robot inter-distance accuracy measures in teach and replay modes. This is due to the fact that this evaluation was limited to neighbor targets located on a specific path and because of the limited reach of the robot to some holes. Table 3 shows the inter-target distance accuracies. For both $\overline{IntDist}_{teach}$ and $\overline{IntDist}_{replay}$, statistically significant differences were observed between the robot operating zones ($p < 0.05$). The pairwise comparisons showed that the inter-target measurement error in zone 4 was significantly higher than in zones 2 and 5 (both with $p < 0.05$). Furthermore, for both $\overline{IntDist}_{teach}$ and $\overline{IntDist}_{replay}$, no significant differences occurred between phantom paths ($p = 0.24$) and between teach and replay modes ($p = 0.60$).

4.3.3. Teach/replay repeatability

Finally, the teach/replay repeatability computed with Eq. (6) was 0.10 ± 0.22 mm. Table 4 summarizes the robot teach/replay repeatability measurements. No significant differences occurred between robot workspace zones ($p = 0.78$) and between different paths ($p = 0.98$) within each zone.

Table 3
Robot inter-distance accuracy

Experimental zones	Phantom paths	$\overline{IntDist}_{teach}$ (mm)	$\overline{IntDist}_{replay}$ (mm)	Sample size (N)
Zone 1	1	0.56 ± 0.43	0.54 ± 0.41	8
	2	0.52 ± 0.23	0.51 ± 0.22	12
	3	0.32 ± 0.16	0.32 ± 0.14	12
	mean	0.45 ± 0.29	0.45 ± 0.27	32
Zone 2	1	0.37 ± 0.13	0.44 ± 0.22	12
	2	0.34 ± 0.28	0.35 ± 0.29	12
	3	0.29 ± 0.21	0.31 ± 0.21	16
	mean	$0.33 \pm 0.21 \delta$	$0.36 \pm 0.24 \delta$	40
Zone 3	1	0.33 ± 0.17	0.33 ± 0.15	12
	2	0.37 ± 0.28	0.35 ± 0.29	12
	3	0.57 ± 0.35	0.59 ± 0.35	16
	mean	0.43 ± 0.30	0.44 ± 0.30	40
Zone 4	1	0.34 ± 0.27	0.34 ± 0.25	12
	2	0.57 ± 0.52	0.61 ± 0.43	12
	3	0.63 ± 0.55	0.61 ± 0.53	16
	mean	$0.44 \pm 0.40 \delta$	$0.47 \pm 0.36 \delta$	40
Zone 5	1	0.26 ± 0.18	0.40 ± 0.30	12
	2	0.48 ± 0.35	0.50 ± 0.35	12
	3	0.27 ± 0.28	0.26 ± 0.27	12
	mean	$0.34 \pm 0.29 \delta$	$0.38 \pm 0.32 \delta$	36
All zones	Total mean	0.43 ± 0.32	0.42 ± 0.33	188

$\overline{IntDist}$ evaluates the robot error in segment length measurements; it is the mean absolute error between the length separating phantom ground truth neighbor points and the length separating the corresponding target points collected with the robot spherical pointer (SP). It was calculated for the robot teach ($\overline{IntDist}_{teach}$) and replay ($\overline{IntDist}_{replay}$) modes. δ indicates a statistically significant difference between experimental zones on pairwise comparisons with $p < 0.05$. No statistically significant difference was found between phantom paths.

Table 4
Robot teach/replay repeatability

Experimental zones	Phantom paths	\overline{Rpt} (mm)	Sample size (N)
Zone 1	1	0.13 ± 0.18	12
	2	0.08 ± 0.10	16
	3	0.04 ± 0.02	16
	Mean	0.09 ± 0.13	44
Zone 2	1	0.18 ± 0.05	16
	2	0.05 ± 0.06	16
	3	0.12 ± 0.22	20
	Mean	0.12 ± 0.26	52
Zone 3	1	0.06 ± 0.04	16
	2	0.16 ± 0.31	16
	3	0.05 ± 0.05	20
	Mean	0.09 ± 0.18	52
Zone 4	1	0.04 ± 0.02	16
	2	0.15 ± 0.15	16
	3	0.20 ± 0.40	20
	Mean	0.14 ± 0.30	52
Zone 5	1	0.10 ± 0.23	16
	2	0.07 ± 0.08	16
	3	0.07 ± 0.15	16
	Mean	0.08 ± 0.16	48
All zones	Total mean	0.10 ± 0.22	248

\overline{Rpt} is the mean teach/replay repeatability which defines the distance between the robot teach and replay points. No statistically significant difference was found between the different zones and paths.

4.4. 3D-US reconstruction of a vascular phantom from a robot scan

4.4.1. Calibration with the cross-wire phantom

The calibration matrix $T_{image}^{USprobe}$ was computed with 62 images at a depth of 6 cm with a cross-wire. The calibration precision C_{rms} achieved was 2.5 mm (see Eq. (8)).

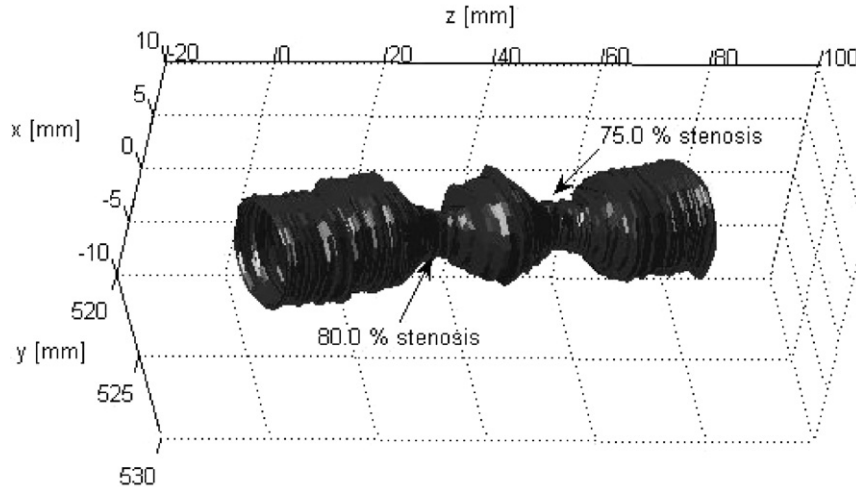


Fig. 9. The 3D-ultrasound reconstructed phantom with double stenoses. Quantification errors of 3.0% and -0.9% were found for the 80% and 75% area reduction stenoses, respectively.

Table 5
Vascular phantom 3D reconstruction results

Vessel parameters	In-vitro phantom	3D reconstruction	Error between the phantom model and the 3D reconstruction
Normal lumen wall diameter	7.98 ± 0.20 mm	7.08 ± 0.36 mm	-0.90 ± 0.16 mm
1st stenosis diameter	3.57 ± 0.20 mm	2.93 mm	-0.64 mm
1st stenosis area reduction ratio	80.0%	83.0%	3.0%
2nd stenosis diameter	3.99 ± 0.20 mm	3.62 mm	-0.37 mm
2nd stenosis area reduction ratio	75.0%	74.1%	-0.9%

4.4.2. 3D-US reconstruction

The phantom with two stenoses was scanned also at a depth of 6 cm. A total of 83 images was captured to reconstruct the vascular phantom. Images were segmented and re-sampled in a $20 \times 20 \times 300$ grid. The surface rendering achieved with the 3D-US system is shown in Fig. 9.

4.4.3. Stenosis evaluation

Table 5 shows quantification errors of 3.0% and -0.9% for the 80% and 75% stenoses, respectively. Additional details on diameter measurements and 3D reconstruction of the phantom are given in Table 5.

5. Discussion

5.1. SP calibration and precision

The SP calibration resulted in a low variability of 0.36 mm (Table 1). Additionally, the precision was close to 0.6 mm over the whole robot workspace indicating an accurate calibration procedure (see Fig. 8). This means that the location of an image acquired with an US probe rigidly attached to the robotic arm handle is expected to be accurately found anywhere in the robot workspace. To assure an accurate SP calibration and constant precision, the robot arm had to be periodically re-homed. This is due to gradual drift in and out of calibration after long periods for which the robot was not operated.

5.2. Performance evaluation

5.2.1. Positioning accuracy

The positioning accuracy was below 0.75 mm for both teach and replay modes (see Table 2). Evermore, it was comparable to the precision of the SP calibration. This observation proves again the consistency of the robot, where the relative positioning accuracy reflects the precision of the robotic arm combined to the precision of the SP calibration procedure. Furthermore, zone 1, the furthest to the robotic arm, showed the worst mean positioning accuracy, as shown in Table 2. When zone 1 was compared to zones 2 and 5, which had the best mean positioning accuracy with values below 0.63 mm, a statistically significant difference was found. The poorer accuracy was due to the mechanical stress in the robotic arm to reach the phantom target points within zone 1. A smaller sample number of 11 target points was indeed used in zone 1 because some targets were out of reach to the robotic arm. While the robot offered an overall acceptable accuracy in its workspace, an optimum setting would be where the robotic arm can reach its target such as in zone 2 or zone 5. Therefore, for a 3D US scan, a patient leg could be placed anywhere in the robot workspace, but the robotic arm positioning accuracy would be better for a leg located within an area closer to its reach.

Concerning the robot scanning paths, the statistical analysis singled out a difference between paths 1 and 3.

This can be observed in Table 2 specifically in zones 3 and 4, where path 3 showed a significant higher positioning error than path 1. Consequently, scanning of tortuous lower limb arterial segments, such as modeled with the curved scanning path 3, does increase the mechanical stress on the robotic arm, however the difference in the positioning accuracy was nevertheless low (≤ 0.20 mm).

5.2.2. Inter-distance accuracy

The inter-distance accuracy was found satisfactory within all robot workspaces (mean accuracy of 0.43 ± 0.32 mm in teach mode and 0.42 ± 0.33 mm in replay mode). In fact, absolute mean distances were always ≤ 0.63 mm. The inter-distance accuracy in Table 3 showed differences between zones. Zone 4 had the largest variations between 0.34 mm and 0.63 mm, and zones 2 and 5 again corresponded to the optimal regions with the lowest variations between 0.26 mm and 0.48 mm. However, no differences were found between the phantom paths. Hence, in the robot workspace, the optimum zones to perform inter-distance evaluation are again zones 2 and 5 where the mean inter-distance accuracies stayed ≤ 0.48 mm. The inter-distance measure is an important parameter as it evaluates the robot error in segment length measurements, which can condition the choice of a therapy (surgical bypass or endovascular approach) and the selection of the length of an angioplasty balloon or a stent.

In both positioning and inter-distance accuracies, the taught and replayed points showed similar results. This confirms, as expected, that the robot can repeat with high accuracy a manually taught trajectory. This is important since the robot can replay at a constant speed the desired scan path for any given patient leg at a high accuracy for 3D reconstruction.

5.2.3. Teach/replay repeatability

The robot teach/replay repeatability reported in Table 4 was found slightly higher than the value specified by the manufacturer, which is 0.05 mm. The higher teach/replay repeatability that reached 0.20 mm might be explained by the calibration procedure of the robot SP. Because the SP was not a fixed component of the robotic system, it became necessary to transform its physical length into the robot referential with Eq. (1). The calibration procedure estimated the SP translation from the robot end-effector. Thereafter all robot point targets were computed with the SP translation estimation to obtain their location in the robot referential. Hence, since SP was involved in all measures of performance, this aspect might explain the difference observed between our study and the manufacturer's specification.

5.3. Comparison to other systems

Precision and inter-distance accuracies obtained in this study were better in comparison to other 3D-US freehand systems evaluated with similar methods. The precision of

these systems was measured as the standard deviation around a target point, which is similar to Eq. (2), and distance accuracies were evaluated according to known phantom inter-target lengths, measurements with a ruler or other referential systems such as robots. The most popular position localizers in 3D-US systems are optical systems and EM sensors.

Optical systems are known to provide the best level of position tracking accuracy. The optical Polaris system (NDI, Waterloo, Ontario, Canada) provided inter-distance errors as low as 0.193 ± 0.167 mm with a precision of 0.059 ± 0.047 mm for a 1 m distance between the camera and the localized object (Khadem et al., 2000). However, these results were obtained only for optimal placement of the optical reflectors with respect to the tracking camera. If not, position accuracies as large as 6.67 mm and mean inter-distance accuracies of 3.55 ± 1.51 mm were achieved (Cartellieri et al., 2001). These last measurements were obtained by using four different optical systems to evaluate the position of a point target on a phantom that was reached with different orientations. In the current study, even though our robot showed an optimum scanning zone and path to reach the best positioning accuracy, and an optimum zone to measure the inter-distance accuracy, the spatial precision was not severely compromised when working in other zones and paths. This would not be the case for optical trackers because the position of the camera would not be optimum to scan, for example, path 1 on the top surface of the phantom and path 3 on its side.

EM position trackers offer the benefit of unrestricted range of motion. However, the accuracy is variable because of their sensitivity to metallic environments and because the transmitter needs to be near the receiver to achieve a good precision. In the literature, there exist discrepancies in the reported precisions and inter-distance accuracies of these devices. Precisions varying between 0.61 mm and 1.7 mm, and inter-distance accuracies varying between 0.05 mm and 1.7 mm, were found for the EM Flock-of-Bird (Ascension Technology, Burlington, Vermont, USA) at distances between the emitter and receiver below 61 cm (Detmer et al., 1994; Hartov et al., 1999; Leotta et al., 1997; Rousseau, 2003). When comparing the Fastrack (Polhemus, Colchester, Vermont, USA) with the Flock-of-Bird system, RMS inter-distance accuracies ranging from 0.21 mm to 1.7 mm, and from 0.16 mm to 1.3 mm were measured, respectively with both systems, at a distance of 30 cm (Rousseau, 2003). In worst case scenarios, for example in clinical settings with EM interferences, inter-distance accuracies as large as 6.4 ± 2.5 mm (Flock-of-Bird) and 3.2 ± 2.4 mm (Fastrack) were obtained for a 9 cm distance between the emitter and receiver (Birkfellner et al., 1998b). For lower limb vessel imaging applications, a setting with metallic objects (e.g., US probe, hospital bed) and typical scanning lengths varying between 50 and 100 cm are expected. Consequently, our robot with a precision of 0.57 ± 0.30 mm (see Fig. 8) and an inter-distance

accuracy of 0.42 ± 0.33 mm (see Table 3) is thus superior to that of approaches using localizing systems since a constant performance can be achieved in all workspaces.

When compared to the few existing robotic 3D-US systems, our design demonstrated its suitability for the proposed clinical application. An articulated mechanical arm for 3D-US imaging had a mean positioning error of 0.7 mm (Hernandez et al., 1996) compared to the position accuracy of 0.62 ± 0.29 mm reported in the current study (see Table 2). With the Hippocrate system (Pierrot et al., 1999), an absolute positioning accuracy of 0.5 mm and a repeatability of 0.05 mm were obtained, which is also similar to our results (a teach/replay repeatability of 0.10 ± 0.22 mm was found with our system, see Table 4). It is to note, however, that a direct comparison with the Hippocrate scanner is difficult because no precise information was available in Pierrot et al. (1999) on how these measures were obtained. Additionally, in this study, no quantitative evaluation of the 3D-reconstruction of an artery was performed. As a result, not much information supports Hippocrate performance in term of validation in a clinical mimicking set up. Our 3D-reconstruction showed quantitatively in Table 5 that the robotic system can quantify stenoses with a good accuracy.

5.4. Advantages and limitations of our robotic system

5.4.1. Performance

In this study, the robot was used as a tracking device to provide positions of 2D-US images for 3D-reconstruction. According to Rousseau (2003), performance of the tracking device includes latency (or lag), update rate, interferences, precision of measures and optimum operating space. To identify how closely a robot follows a taught scan pattern determined by a clinician, it is first important to discuss latency and update rate. Latency is the delay required for the system to detect motion. Update rate refers to the number of positions reported by the system per second. Unfortunately, no measurements of these characteristics were performed or disclosed by the manufacturer of our robotic system. Nevertheless, we did not observe any limitations in scanning mimicking arteries and we can assume that latency and update rate frequencies are faster than the frame rate of US scanners (typically 30 Hz for most applications). Consequently, we do not anticipate any problems for lower limb vessel scanning by a clinician.

Interferences affecting the robot performance can occur when the operating environment is not respected (i.e., temperature, humidity and extreme electrical noise). Accordingly, the environment for the current study encompassed the manufacturer operative conditions required to preserve robust performances (i.e., room temperature and humidity, and normal electrical interferences encountered in industries or hospitals).

For robotic 3D-US imaging, precision of measures and resolution of US images should be comparable. At 10 MHz, US image resolution has approximately, at

3 cm depth, a resolution of 0.3–0.4 mm in axial, 1.0–2.0 mm in lateral and 3.0–4.0 mm in out of plane orientations (Dajani, 2000). In our study, the positioning accuracy of the robot (≤ 0.75 mm) was similar to the combined axial and lateral resolutions of US imaging. However, since the sensing technology of the arm relies on the transformation of joint angles into the end-effector position, the robotic arm will maintain a reliable performance in complex movements if the robot joints are operated within the safe boundary of their limits. It is to note that binding of the arm is very unlikely because our design is based on a robust industrial robot. However, excessive vibrations may limit the performance.

Other performance limitations include the use of the system under clinical conditions for scanning patients of different anatomy. Currently, our robotic system is limited to accommodate each scan of a patient's leg with a manual taught path made by a clinician. Henceforth, the robot replays this path over the leg and acquires at a constant step US image planes based on a pre-determined trajectory. Of course, movement of the patient's leg between the taught and replay modes would eventually need to be addressed. The patient leg may be either immobilized or an automatic tracking of the vessel and registration during replay may be required. However, these solutions are beyond the scope of the present article.

Finally, the robot performance was evaluated for position and inter-distance accuracies and for teach/replay repeatability at different locations within its operating workspace. A map zone that characterizes the robot performance limitations inside its workspace was achieved (see Fig. 5 and Tables 2–4). It was found that the robot positioning accuracy limits varied between 0.46 mm and 0.72 mm, the inter-distance accuracy boundaries were between 0.26 mm and 0.63 mm, and the teach/replay repeatability was from 0.04 mm to 0.20 mm. Thus, a clinician can generally expect these performances when operating inside the robot workspace during the scanning of a patient.

5.4.2. Design

In this study, we identified the limits of accuracy from the base of the robotic arm that extends to SP for scanning lower limbs. The level of accuracy we can achieve with our robotic system is greatly influenced by the mechanical design specifications of the robotic arm. More specifically, the number of mechanical joints and link dimensions (i.e., member lengths of the robotic arm) are significant elements. Including SP in the evaluation certainly reduced the reported accuracy of our robotic system. It would be possible to improve accuracy with SP by adding mechanical joint limits to the robotic arm to restrain the workspace for optimal operation (Duchemin et al., 2004). An alternate way to improve and preserve performance would be to change the physical design of the robotic arm by computing a model of optimal link dimensions and joint orientations (i.e., kinematic parameters) with SP. The Jacobian, a matrix that depends on a kinematic model to relate joint

velocities to the end-effector, would be a solution to provide a better positioning accuracy measured at the end-effector with SP (Mavroidis et al., 1998).

Elastic joints are another source that can influence the level of accuracy achievable by a robot. Under this assumption, our robot has intrinsic compliant elements at the joints (e.g., six revolute joints, F/T sensor and cables) that have to be considered. Elasticity of mechanical transmission is often the cause of positional errors at the end-effector when a robot works in contact with the environment (Zollo et al., 2005). This is often due to static deformations caused under gravity in position tracking and interaction tasks. Given our robotic system was designed to interact with humans, and was in contact with a lower limb mimicking phantom for this study, this aspect is thought to be important to explain the reported positioning accuracies. Nonetheless, when the robot interacts with humans, these effects can be reduced to ensure a high performance with the design of a compliance control in the Cartesian space of the robotic system.

5.5. 3D-reconstruction of a vascular phantom from a robot scan

5.5.1. Calibration with a cross-wire and 3D-US reconstruction

The calibration matrix obtained with the cross-wire showed a precision suitable for a preliminary 3D-reconstruction. However, the calibration precision affected the geometry of the reconstructed vessel in the longitudinal axis. This can be seen in Fig. 9, where the 3D reconstruction is slightly shifted in the $x - y$ plane along its length (z axis). It is important to remember that the vascular phantom had a symmetric geometry along its length. For future work, we expect that it may be feasible to improve the calibration precision as the accuracy of the method relies on how well the intersecting point can be detected in the B-scan images and on how the cross-wire location can be precisely estimated in the robot referential. While the precision affected the 3D reconstructed central axis, it did not seem to influence severely the overall geometry. Thus, the stenosis severity could satisfactorily be evaluated from the 3D volume. Nevertheless, a better accuracy than 3.0% (see Table 5) may be expected and a z -phantom calibration device may be a solution for this problem (Mercier et al., 2005).

5.5.2. Stenosis evaluation

Imaging lower limb stenoses is an important application for 3D-US. This non-invasive imaging technique may become an alternative to 3D reconstruction of arterial segments obtained with magnetic resonance imaging and computed tomography angiography. Carotid artery atherosclerotic plaque progression was evaluated in patients with a 3D-US linear step motor system (Delcker and Diener, 1994). Already, the vascular risk factors promoting plaque progression were monitored and analyzed

with this system (Delcker et al., 1995). Another study validated the 3D-US Flock-of-Bird EM system to measure a phantom and blood conduit geometries (Hodges et al., 1994). Dimensions of uniform and stenotic 3D-reconstructed phantoms were measured. This system was able to detect diameter reductions up to 28% corresponding to an area reduction of 48%. More recently, a study with a similar EM system evaluated the error in stenosis quantification for the 3D-US reconstruction of carotid bifurcation phantoms and found errors of -1.2% for detecting a 70% stenosis (Barratt et al., 2004). We found similar results with errors of 3.0% for detecting a 80% stenosis, and errors of -0.9% for quantifying a 75% stenosis (see Table 5).

6. Conclusion

The prototype medical robot proved to be a suitable tracking device that offers a constant performance and control to acquire 3D positions with a high precision, and good position and inter-distance accuracies. The computed positions in the robot referential of the acquired US images were satisfactory to quantify stenoses in a 3D reconstructed vessel phantom. Of course, further developments and validations of the robotic system are necessary to provide a platform that would meet clinical needs. Developments include a more robust 3D-US image calibration procedure to improve the accuracy of the 3D reconstruction from B-mode, color and power Doppler images. The integration of electrocardiogram data in the robot control system to gate the US image acquisition would also eliminate deformations of the reconstructed volume due to the pulsation of the vessel wall. Acquisition of US images with controlled applied pressure may also be of interest to enable non-invasive elastographic measurements of pathological biological tissues (Maurice et al., 2004) or to detect deep venous thrombosis with objective vessel compression measures (Guerrero et al., 2006).

Acknowledgements

This work was supported in part by the Canadian Institutes of Health Research (CIHR) under grant MOP #53244. Drs. Soulez and Cloutier are, respectively, recipient of a Clinical Research Scholarship Award and of a National Scientist Award of the Fonds de la Recherche en Santé du Québec. Ms. Janvier is recipient of Studentship Awards of the Fonds de la Recherche sur la Nature et les Technologies du Québec and of the Quebec Black Medical Association, whereas the salary of Ms. Roy Cardinal is partially supported through a Studentship Award of the Natural Sciences and Engineering Research Council of Canada. The authors are grateful to Dr. Louise Allard for manuscript revisions, and to Mr. Benoit Godbout of the University of Montreal Hospital and Dr. Daniel Leotta of the University of Washington for helpful discussions.

References

- Abolmaesumi, P., Salcudean, S.E., Zhu, W.-H., Sirouspour, M.R., DiMaio, S.P., 2002. Image-guided control of a robot for medical ultrasound. *IEEE Transactions on Robotics and Automation* 18 (1), 11–23.
- Barratt, D.C., Davies, A.H., Hughes, A.D., Thom, S.A., Humphries, K.N., 2001. Accuracy of an electromagnetic three-dimensional ultrasound system for carotid artery imaging. *Ultrasound in Medicine and Biology* 27 (10), 1421–1425.
- Barratt, D.C., Ariff, B.B., Humphries, K.N., et al., 2004. Reconstruction and quantification of the carotid artery bifurcation from 3-D ultrasound images. *IEEE Transactions on Medical Imaging* 23 (5), 567–583.
- Birkfellner, W., Watzinger, F., Wanschitz, F., et al., 1998a. Calibration of tracking systems in a surgical environment. *IEEE Transactions on Medical Imaging* 17 (5), 737–742.
- Birkfellner, W., Watzinger, F., Wanschitz, F., et al., 1998b. Systematic distortions in magnetic position digitizers. *Medical Physics* 25 (11), 2242–2248.
- Bushberg, J.T., Seibert, J.A., Leidholdt Jr., E.M., Boone, J.M., 2002. *The Essential Physics of Medical Imaging*, 2nd ed. Lippincott Williams & Wilkins, Philadelphia, Chapter 6, pp. 469–565.
- Cartellieri, M., Vorbeck, F., Kremser, J., 2001. Comparison of different 3D navigation systems by a clinical user. *Acta Archives of Otolaryngology* 258, 38–41.
- Cloutier, G., Soulez, G., Qanadli, S.D., Teppaz, P., Allard, L., Qin, Z., Cloutier, F., Durand, L.-G., 2004. A multimodality vascular imaging phantom with fiducial markers visible in DSA, CTA, MRA, and ultrasound. *Medical Physics* 31 (6), 1424–1433.
- Dajani, K.F., 2000. Analysis of carotid and femoral stenosis and lesions with three-dimensional ultrasound, Ph.D. thesis, The University of Toledo, Ohio, USA.
- Delcker, A., Diener, H.C., 1994. Quantification of atherosclerotic plaques in carotid arteries by three-dimensional ultrasound. *The British Journal of Radiology* 67 (799), 672–678.
- Delcker, A., Diener, H.C., Wilhelm, H., 1995. Influence of vascular risk factors for atherosclerotic carotid artery plaque progression. *Stroke: American Heart Association* 26, 2016–2022.
- Detmer, P.R., Bashein, G., Hodges, T., Beach, K.W., Filer, E.P., Burns, D.H., Strandness Jr., D.E., 1994. 3D Ultrasonic image feature localization based on magnetic scanhead tracking: in vitro calibration and validation. *Ultrasound in Medicine and Biology* 20 (9), 923–936.
- Duchemin, G., Maillet, P., Poignet, P., Dombre, E., Pierrot, F., 2004. Medically safe and sound. *IEEE Robotics and Automation Magazine* 11 (22), 46–55.
- Elsman, B.H., Legemate, D.A., de Vos, H.J., Mali, W.P., Eikelboom, B.C., 1997. Hyperaemic colour duplex scanning for the detection of aortoiliac stenoses. A comparative study with intra-arterial pressure measurement. *European Journal of Vascular and Endovascular Surgery* 14 (6), 462–467.
- Fenster, A., Downey, D.B., 2000. Three-dimensional ultrasound imaging. *Annual Review of Biomedical Engineering* 2, 457–475.
- Frantz, D.D., Wiles, A.D., Leis, S.E., Kirsh, S.R., 2003. Accuracy assessment protocols for electromagnetic tracking systems. *Physics in Medicine and Biology* 48, 2241–2251.
- Golledge, J., 1997. Lower-limb arterial disease. *Lancet* 350 (9089), 1459–1465.
- Gonzales, A.V., Cinquin, P., Trocraz, J., Guerraz, A., Hennion, B., Pellissier, et al., 2001. TER: a system for robotic tele-echography. *MICCAI* 2001, 1–8.
- Guerrero, J., Salcudean, S.E., McEwen, J.A., Masri, B.A., Nicolaou, S., 2006. System for deep venous thrombosis detection using objective compression measures. *IEEE Transactions on Biomedical Engineering* 53 (5), 845–854.
- Hartov, A., Eisner, S.D., Roberts, D.W., Paulsen, K.D., Platenik, L.A., Miga, M.I., 1999. Error analysis for a free-hand three-dimensional ultrasound system for neuronavigation. *Neurosurgical Focus* 6 (3), Hernandez, A., Basset, O., Chirossel, P., Gimenez, G., 1996. Spatial compounding in ultrasonic imaging using an articulated scan arm. *Ultrasound in Medicine and Biology* 22 (2), 229–238.
- Hodges, T.C., Detmer, P.R., Burns, D.H., Beach, K.W., Strandness Jr., D.E., 1994. Ultrasonic three-dimensional reconstruction: in vitro and in vivo volume and area measurement. *Ultrasound in Medicine and Biology* 20 (8), 719–729.
- Khadem, R., Yeh, C.C., Sadeghi-Tehrani, M., Bax, M.R., 2000. Comparative tracking error analysis of five different optical tracking systems. *Computer Aided Surgery* 5, 98–107.
- Leotta, D.F., Detmer, P.R., Martin, R.W., 1997. Performance of a miniature magnetic position sensor for three-dimensional ultrasound imaging. *Ultrasound in Medicine and Biology* 23 (4), 597–609.
- Matignon, Y., 2002. Échographie-Doppler dans l'artériopathie oblitérante des membres inférieurs. [http://www.anaes.fr/anaes/Publications.nsf/nPDFFile/RA_LILF-5EHJD7/\\$File/echodoppler.rap.pdf](http://www.anaes.fr/anaes/Publications.nsf/nPDFFile/RA_LILF-5EHJD7/$File/echodoppler.rap.pdf). Agence Nationale d'Accréditation et d'Évaluation en Santé [Juin], pp. 1–144. Consulted 7-14-2004.
- Maurice, R.L., Ohayon, J., Fretigny, Y., Bertrand, M., Soulez, G., Cloutier, G., 2004. Noninvasive vascular elastography: theoretical framework. *IEEE Transactions on Medical Imaging* 23 (2), 164–180.
- Mavroidis, C., Flanz, J., Dubowsky, S., Drouet, P., Goitein, M., 1998. High performance medical robot requirements and accuracy analysis. *Robotics and Computer-Integrated Manufacturing* 14, 329–338.
- McDermott, M.M., Greenland, P., Liu, K., Guralnik, J.M., Celic, L., Criqui, M.H., Chan, C., Martin, G.J., Schneider, J., Pearce, W.H., Taylor, L.M., Clark, E., 2002. The ankle brachial index is associated with leg function and physical activity: the walking and leg circulation study. *Annals of Internal Medicine* 136 (12), 873–883.
- Mercier, L., Lango, T., Lindseth, F., Collins, L.D., 2005. A review of calibration techniques for freehand 3-D ultrasound systems. *Ultrasound in Medicine and Biology* 31 (2), 143–165.
- Mooring, B.W., Roth, Z.S., Driels, M.R., 1991. *Fundamentals of Manipulator Calibration*. John Wiley & Sons Inc., New York.
- Nelson, T.R., Pretorius, D.H., 1998. Three-dimensional ultrasound imaging. *Ultrasound in Medicine and Biology* 24 (9), 1243–1270.
- Pierrot, F., Dombre, E., Dégoullange, E., Urbain, L., Caron, P., Boudet, S., Gariépy, J., Mégrien, J.-L., 1999. Hippocrate: a safe robot arm for medical applications with force feedback. *Medical Image Analysis* 3 (3), 285–300.
- Rousseau, F., 2003. Méthodes d'analyse d'image et de calibration pour l'échographie 3D en mode main-libre", Ph.D. Thesis., Institut de Formation Supérieure en Informatique et Communication, VISTA (IRISA, RENNES), December 15th 2003.
- Roy Cardinal, M.H., Meunier, J., Soulez, G., Maurice, R.L., Therasse, E., Cloutier, G., 2006. Intravascular ultrasound image segmentation: a three-dimensional fast-marching method based on gray level distributions. *IEEE Transactions on Medical Imaging* 25 (5), 590–601.
- Sonix ultrasound system, User manuel, Ultrasonix Medical Corporation, Sonix series ultrasound system, Burnaby, B.C., Canada, October 2005. <http://www.ultrasonix.com>.
- Tseng, C.-S., Huang, C.-C., Chen, C.-S., 2007. Development of an image-guided robotic system for surgical positioning and drilling. *Robotica* 25, 375–383.
- Weitz, J.I., Byrne, J., Clagett, P., Farkouh, M.E., Porter, J.M., Sackett, D.L., Strandness Jr., D.E., Taylor, L.M., 1996. Diagnosis and treatment of chronic arterial insufficiency of the lower extremities: a critical review. *Circulation* 94, 3026–3049.
- Zhouping, W., Gardi, L., Downey, D.B., Fenster, A., 2005. Oblique needle segmentation and tracking for 3D TRUS guided prostate brachytherapy. *Medical Physics* 32, 2928–2941.
- Zollo, L., Siciliano, B., DeLuca, A., Guglielmelli, E., Dario, P., 2005. Compliance control for an anthropomorphic robot with elastic joints: theory and experiments. *Transactions of the ASME. Journal of Dynamic Systems, Measurement and Control* 127 (3), 321–328.